

# Printable Graphene–Insulator–Semiconductor (GIS) Heterostructures for Active Control of Infrared Q-Switched Laser

Tengfei Dai, Jianhua Chang,\* Hongxu Li, Sian Chen, Haiyang Liu, Youlin Xia, Zheng Peng, Zhi Tao, Hai Hu,\* and Xiang Liu\*

2D materials have recently attracted extensive attention in solid-state laser devices due to the improvement of their beam quality and service life. However, most conventional devices suffer from the fixed saturable absorption properties of certain 2D materials and are confined to the determined operation state. Herein, on-chip electrically tunable infrared laser signals are realized by introducing a novel 2D nanomesh saturable absorber (SA) interaction layer without other tuning elements based on printable graphene–insulator–semiconductor (GIS) heterostructures. The pulse width can be highly controllable ranging from 1  $\mu$ s to 360 ns under ultralow electrical modulation power ( $\approx 10$  pA current and  $< 0.5$  nW power), thanks to the high conductivity and tunability of graphene. Furthermore, the precise regulation mechanism of the Fermi level of graphene by the heterostructures is comprehensively explored through opto-electrical characterization with spectroscopic methods. The GIS device introduces a promising way to achieve actively controlled solid-state optoelectronic and nonlinear photonic devices in the future.

absorber (SA) for ultrafast laser systems derived from its  $\pi$ – $\pi$  band structure with dirac point.<sup>[6–8]</sup> Moreover, the possibility of novel 2D nanosheet would allow the facile ultrafast photonics for passively-controlled Q-switched<sup>[9]</sup> or mode-locking<sup>[10]</sup> laser systems, such as Ag<sub>2</sub>S nanosheets,<sup>[11]</sup> 2D TiS<sub>2</sub>,<sup>[12]</sup> 2D FeS<sub>2</sub>,<sup>[13]</sup> bismuthine,<sup>[14]</sup> and 2D perovskite nanosheets.<sup>[15]</sup> Therefore, proposing the novel device structures incorporation<sup>[16]</sup> of the new-type 2D SA materials may be an important step toward future low-power and easy-modulated ultrafast laser system.

It is worth noting that the GIS device can achieve substantial modification of the optical absorption of graphene directly by tuning the Fermi level with an electrical signal.<sup>[17–20]</sup> For example, the all-fiber graphene devices have been demonstrated a significant optical transmission change

(>90%) with electrical gating.<sup>[21]</sup> Although the results are promising, gate-controlled Q-switched solid-state lasers have not yet been realized due to the challenging of ultrathin functional layer and free space light's propagation. In addition, some important and preliminary findings presented in recent published papers have demonstrated tunable pulse width and wavelength Q-switched laser systems through direct pumped modulation with high electrical power or other bulk tuning elements' assistance.<sup>[22–25]</sup> Therefore, additional research on the efficient active on-chip electrical control of entire-solid-state laser systems needs to be implemented.

We demonstrate an electrically active controllable solid-state laser with a graphene–Si<sub>3</sub>N<sub>4</sub>–In–Ga–Zn–O (IGZO) vertical solid-state electronic device as a solid-to-solid (STS) SA on-chip device, which serve as an on-chip electrically tunable inline nonlinear SA functioning within a  $\approx 1$   $\mu$ s to 360 ns pulse width by integration into the ultrafast Q-switched laser system. The peculiar GIS structure is built on a quartz substrate, where IGZO and nanomeshed graphene (N-gra) play crucial roles as extremely efficient semiconductor gating medium.<sup>[26–28]</sup> The Q-switched laser pulse is generated by the N-gra component of GIS device due to its nonlinear absorption characteristics. As an infrared-blind semiconductor, IGZO active layer can also exhibit extremely high on/off ratio for typical electron devices, such as metal–oxide–semiconductor (MOS) and field-effect-transistor

## 1. Introduction

Graphene–insulator–semiconductor (GIS) hetero-junctions have recently received substantial attention due to their long operating lifetime, high efficiency, and outstanding electrical modulation ability.<sup>[1–3]</sup> To date, vertical structures based on pristine and nanopatterned graphene films have emerged for electrical applications in high-performance optical modulator,<sup>[4]</sup> electronic storage devices,<sup>[5]</sup> and field-effect tunneling transistors.<sup>[6]</sup> As a high mobility 2D material, graphene and its heterostructure can be operated as a widely cross-band Saturable

Dr. T. Dai, Prof. J. Chang, Dr. H. Li, S. Chen, H. Liu, Y. Xia, Z. Peng,  
Dr. Z. Tao, Prof. X. Liu

School of Electronics and Information Technology  
Nanjing University of Information Science and Technology  
Nanjing 210096, China  
E-mail: jianhuachang@nuist.edu.cn; xjlx1906@126.com

Prof. H. Hu  
CAS Center for Excellence in Nanoscience  
National Center for Nanoscience and Technology  
Beijing 10010, China  
E-mail: huh@nanoctr.cn

 The ORCID identification number(s) for the author(s) of this article can be found under <https://doi.org/10.1002/adom.202001502>.

DOI: 10.1002/adom.202001502

(FET) devices.<sup>[26,27]</sup> Due to the high transparency derived from its plasma frequency in the infrared region,<sup>[29,30]</sup> the  $\text{Si}_3\text{N}_4$  insulator can both guarantee the laser penetration and suppress the operating current to obtain low modulating power. Additionally, the piezoelectric inkjet printing of silver ion ink provides an easy drop-on-demand and well-positioned method for the alignment and formation of silver contacts on GIS devices.

## 2. Device Design and Characterization

As illustrated in **Figure 1a**, the GIS transistor with top-contact calibrated electrodes is fabricated as follows: graphene is initially grown on a  $\text{SiO}_2$  Quartz substrate by a plasma-enhanced chemical vapor deposition (PECVD) process. To deposit a high-quality few-layer graphene film, a combination of growth parameters are precisely controlled (700 °C growth tempera-

ture, 300 mTorr stable gas pressure, 200 W plasma power, and 22 min deposition time). Additionally, AAO (Anodic Aluminum Oxide) membrane with PMMA film is transferred on the top of the few-layer graphene. Reaction ion etching (RIE) approach is used to form the nanomesh as shown in the image of **Figure 1f,g**, with optimized 200 nm gaps diameter to achieve high optical-electrical performances (**Figure S2d**, Supporting Information). A fast method is demonstrated for the deposition of highly conductive silver and IGZO semiconductor features using a drop-on-demand piezoelectric IJP system (a multifunctional scientific printing machine from Shanghai Prtronic Ltd.). This is immediately followed by the deposition of 160 nm thick  $\text{Si}_3\text{N}_4$  insulator onto the heterostructure by room-temperature PECVD. The IGZO and high quality  $\text{Si}_3\text{N}_4$  film's morphology deposited on the graphene can be observed through the atomic force microscopy (AFM) image as shown in **Figure S1** in the Supporting Information.

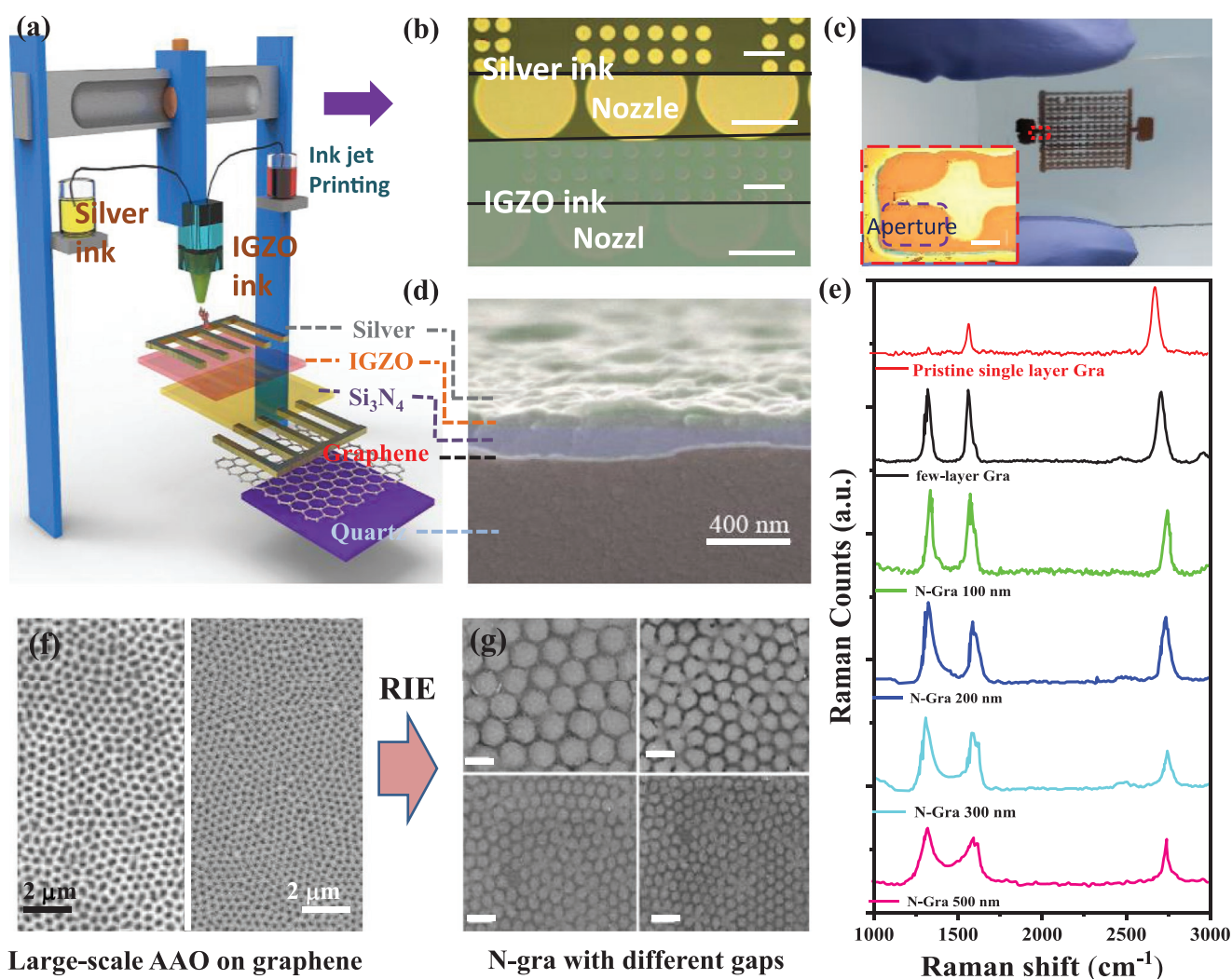


**Figure 1.** a) Schematics of the as-fabricated GIS aperture by ink-jet printing production processes. b) Neat and precise print array of 16 nozzles for silver pad and IGZO ink respectively (scale bar: 80, 20, 200, 80  $\mu\text{m}$ ). c) Top-view image of the GIS device and (inset) optical microscopy image of the device with metal-oxide, insulator and metal electrodes fabricated by inkjet printing (scale bar: 100  $\mu\text{m}$ ). d) Cross-sectional SEM cross-sectional images (scale bar: 400 nm) of the GIS aperture. e) Raman spectra of pristine single layer graphene, few-layer graphene and N-gra (with 100, 200, 300, and 500 nm gaps). f) AAO images with two different wholes on the surface of few-layer graphene. g) SEM morphology images of etched N-gra layers with 200, 300, 400, and 500 nm gaps.

The IGZO ink is prepared by combining zinc acetate dihydrate, gallium nitrate hydrate, and indium nitrate hydrate in 2-methoxyethanol (2ME) solvent. As shown in the top-view cross-sectional scanning electron microscopy (SEM) images of Figure 1d, the oxide semiconductor (IGZO) is printed as the top modulated semiconductor. Through our excimer laser's annealing after-treatment ( $308\text{ nm}$ ,  $300\text{ mJ cm}^{-2}$ ), the average granules' size increases as illustrated in Figure S1 in the Supporting Information, which brings the extraordinary electrical performance such as high mobility ( $8\text{--}25\text{ m}^2\text{ V}^{-1}\text{ s}^{-1}$ ), low off current, and high subthreshold slope (S.S.).<sup>[28,31]</sup>

Raman spectroscopy (Figure 1e) measurements are used to characterize the atomic structures of the fabricated graphene films. Compared with pristine materials, the graphene in our work has a typical 2D few-layered structure, while the etched N-gra exhibits obvious P-type semiconductor property from the enhanced D peak.<sup>[29,32]</sup> That comes from the extra oxygen defects at the edge of the N-gra. As shown in Figure 2c, the transmission characteristics of the materials are investigated with a UV–vis–NIR spectrophotometer.

Because this vertical device should provide applicable optical testing windows, the following design criteria should be taken into consideration: (i) guarantee the transparency of the heterostructures to create an infrared optical transmission laser aperture (as shown in Figure 2c; (ii) optimize the GIS structures to ensure effective electrical modulation. Ab initio numerical simulations are carried out to analysis charge distribution intensity ( $\rho_c$ ,  $\text{C }\mu\text{m}^{-2}$ ) within the GIS structures by the finite element method (FEM). The Charge distribution density of winged electrodes is better than that without

wings (Figure S2a, Supporting Information) due to the field enhancement effect. Furthermore, as the distance between two contacts decreases, the intensity of the charge is substantially enhanced. To better match the design criteria, the influences of different distances between two contacts are simulated and tested (Figure 2d–f). Shorter distances show higher charge density concentrations and better modulation ability as well as a higher risk of electronic breakdown as depicted in Figure 2f.

It is worth optimizing the layout of the aperture, and the carrier concentration along the light transmitting route will decrease and result in faint interactions. Corresponding with the simulated results, the completed GIS aperture can be observed in the top-view optical microscopy image of the GIS device (Figure 1c). Taking into account our process conditions and the above principles (Figure 2d), an optimized distance (gap) of  $80\text{ }\mu\text{m}$  is confirmed. Consequently, we experimentally demonstrate the appropriate distance between the electrodes due to a certain distance exhibiting excellent optical and electrical properties, which can obtain a shorter pulse width (the laser power at a certain value of the duration) in Q-switched laser systems. In addition, the different GIS heterostructures with  $20\text{--}100\text{ }\mu\text{m}$  gaps were measured (IGZO-semiconductor is connected to applied voltage and graphene is ground connection) by semiconductor analyzer as shown in Figure 2d. With the assistance of the silicon nitride insulator, our device can achieve an ultra-low operated current ( $100\text{ pA}$ ) at high gate voltage ( $\pm 40\text{ V}$ ). These experiments can demonstrate that our device can guarantee the intense charges' accumulation but not create leakage current at this scale.

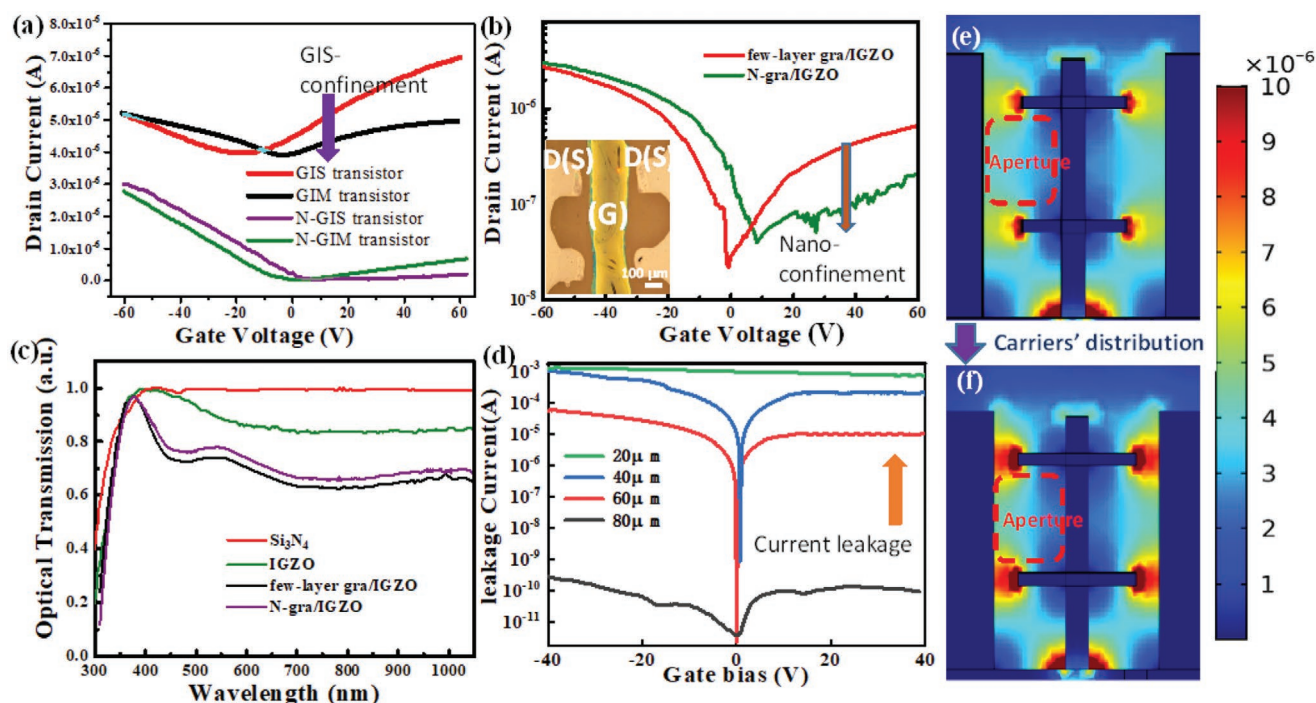


**Figure 2.** a) Transfer characteristics of GIS and GIM under  $0.1\text{ V }V_{ds}$  with and without nanomesh structures. b) Transfer  $IV$  curves of the few-layer/IGZO and N-gra/IGZO devices under  $0.1\text{ V }V_{ds}$  (inset: the measured device's image with two top-electrodes as drain/source). c) Optical transmission properties of the different material layers of the GIS device. d) Leakage current versus gate bias under different electrode layouts. e, f) Simulated distribution of the carriers of different electrode structures in the GIS aperture.

### 3. Results and Discussion

The insulator and capacitance are among the most crucial elements and play an important role in charge density, current's limitation and gate modulation.<sup>[33,34]</sup> To fully analyze the operating mechanism of this optical aperture, typical  $C-V$  and  $I-V$  characteristics of the GIS structure are investigated to compare with other similar structures (as shown in Figure S3a,d in the Supporting Information). Graphene normally behaves as a semi-metal with zero bandgap alignment. For graphene-insulator-metal (GIM) structures both for few-layer and N-gra devices, it is difficult to modulate a "parallel-plate" like capacitor with metallized graphene and metal electrodes due to the constant permittivity. In contrast, the semiconductor oxide (IGZO) buffer layer is vital to improve the electrical modulation capability.

As exhibited in Figure 2a,b, the further study on the impacts of the nanomesh is also carried. The transfer  $IV$  curves of the splicing two heterostructure devices are investigated in Figure 2b. Due to the introducing of bandgap, the on/off ratio of p-type device with N-gra active layer is nearly 1 decade order larger compared with the few-layer graphene counterpart.

For solid-state pulsed laser studies, a passively Q-switched Nd:YVO<sub>4</sub> laser device is typically fabricated for generating laser pulses ranging from microseconds to nanoseconds with a SA. In this work, the STS SA heterostructure can overcome the discrete nature of nonlinear saturable absorption in graphene

sheets with the applied gate voltage. To experimentally confirm the feasibility of the application as an electrically controllable nonlinear SA, we built a Q-switched operation, as shown in schematic of Figure 3a and practical experiments image of Figure S4b in the Supporting Information. The 5-mm-long Nd:YVO<sub>4</sub> with a doping concentration of 0.5 at% and a cross section of  $3 \times 3 \text{ mm}^2$  is used as a gain medium.

The laser crystal is optically pumped by a fiber-coupled semiconductor laser with a central output wavelength of 1064 nm (fiber core diameter: 400  $\mu\text{m}$ ; numerical aperture: 0.22). Lastly, by using a fiber optic spectrometer (Seemantech S3000-VIS), the central wavelength of the laser output is measured at 1064.2 nm without applied gate voltage). As shown in inset mapping image of Figure S4b in the Supporting Information, ABCD matrix analysis revealed and demonstrated that the beam radii at the center of the laser crystal and SA are 211 and 204  $\mu\text{m}$ , respectively. To promote cavity efficiency, a 1:1 coupling system is employed to climatize and focus the pump light into the laser crystal (beam radius: 200  $\mu\text{m}$ ). A 25 °C water cooling system is a powerful way to efficiently reduce the thermal effect, which is performed by wrapping the laser crystal with indium foil and mounting it on a copper holder. The measured pulse duration of the Q-switched operation can be received by a fast photodiode (Newport Model 818-BB-21), showing that it has a rising time of 250 ps and can be recorded by a digital oscilloscope with a bandwidth of 500 MHz. It shows a maximum output performance variation in the passive Q-switched operation at high positive

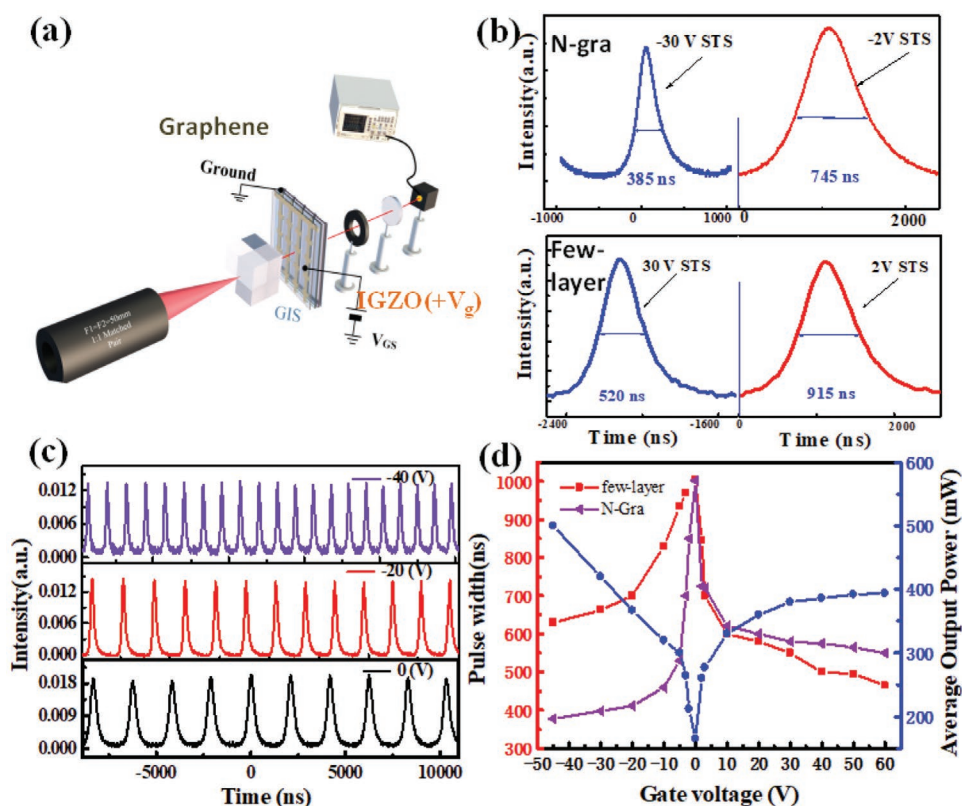


**Figure 3.** a) Experimental setup of the passively Q-switched Nd:YVO<sub>4</sub> laser. b) The enlarged waveform of the pulse for both few-layer and N-gra based devices under different applied gate voltages. c) The waveforms of the Q-switched laser at different gate biases. d) The pulse width and the average output power versus the gate voltage of few-layer graphene and N-gra based devices.

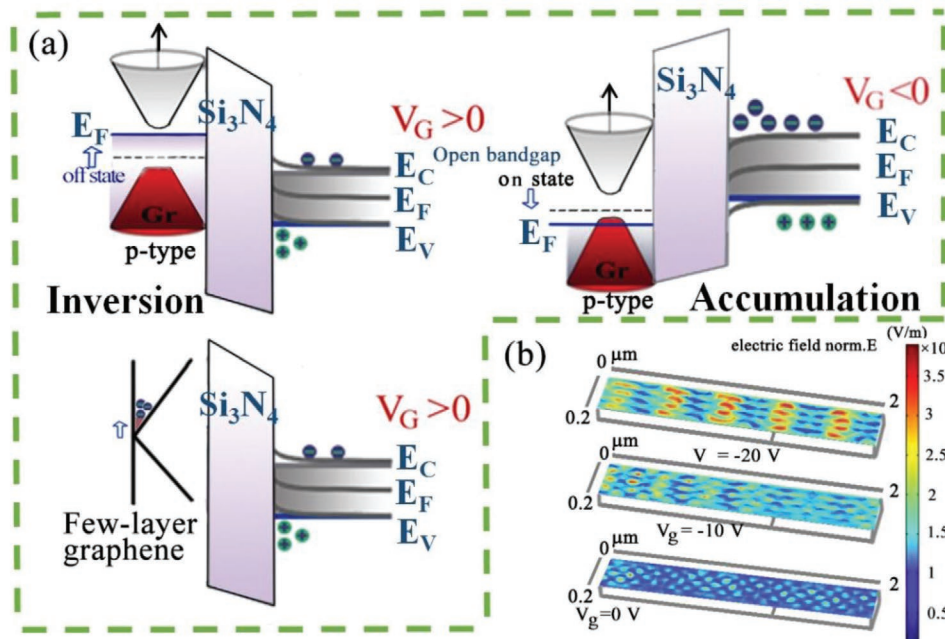


**Figure 4.** a) Schematics of device physics. b) Semiconductor-electromagnetic Multiphysics simulation for the device with different gate voltages.

voltage. And the effective on-chip pulse width modulation of laser can be observed at Figure 3c with responded waveforms under different applied gate voltages.

The extreme duration can be regulated to 385 ns at a 30 V amplitude ( $V_g$ : -30 V) modulated voltage for N-gra GIS device. In contrast, the few-layer based GIS device can only reach at 520 ns at the same 30 V amplitude ( $V_g$ : 30 V) as shown in Figure 3b. Obviously, the device with etched N-gra SA presented more efficient gate modulation, which also brings about much smaller operation gate voltage amplitude. Because of the proved limited current ( $\approx 10$  pA) derived from the Si<sub>3</sub>N<sub>4</sub> dielectric, the extreme modulating power is less than 0.5 nW. As can be explained in Figure 3d, the variation in the pulse is mainly relevant to the gate voltage when the absorbed pump power is constant at 1.67 W, most likely due to the optical transmission change in graphene. The pulse average output power can be modulated from 120 to 530 mW directly with gate voltage (within a limited voltage range), but the pulse width presents a similar inverse variation derived from the compressed pulse waveforms.

Figure 4a schematically shows the energy level modulation mechanism of the vertical GIS from the heterojunction bandgap alignment. Obviously, compared with the zero band few-layer graphene, N-gra can open the zero-band gap of graphene and enhance the carrier's distribution by gate voltage's modulation. It creates enhanced optical-electrical interaction from the quantum confinement. To research the gate voltage's modulation, the semiconductor-electromagnetic numerical model simulates a simple nanomesh heterostructure (illustrated in the Figure 4b). Without gate voltage, the light field cannot exhibit a clear distinction between graphene and dielectric medium. There is a discernible field enhancement effect at the graphene segment due to the carrier's distribution by the gate control.

To further exploit the optical-electrical performance of the GIS heterostructure with N-gra, the optical absorption intensity is measured by varying the gate voltage's amplitude (Figure 5a). The optical spectrum demonstrates the effective interactions between gate modulation and light absorption. It can be seen that the absorbency of the GIS device is significantly enhanced following the previous increase in the gate voltage amplitude. By contrast, the compared device with few-layer graphene shows weak effects versus the variation in gate voltage at infrared region, as depicted at Figure S3b in the Supporting Information. Additionally, the slight blue shift for the absorbance spectra can be found in this optical-electrical characterization (as shown in Figure S2e in the Supporting Information). The blue shift of laser's output spectra is determined by the dielectric index of the media along the propagation path and photo-thermal effect of graphene nanosheet,<sup>[25]</sup> which can be adjusted by the GIS structures. Thus, we keep the laser power fixed and only modulate the device's gate voltage to obtain the tuning range of wavelength from 1064.2 to 1062.08 nm (as illustrated in the gate-dependent output laser spectra of Figure 5b). Owing to the significant shift in the Fermi level, the optical transmission and emission spectra of the device are controlled by electrical bias. The influence of the optical nonlinear properties can surmount the discrete nature of nonlinear absorption in normal bulk graphene.<sup>[17,20,21]</sup>

As demonstrated in the C-V electrical and photoinduced IV characterization of Figure S3c,d (Supporting Information), the photogenerated carriers can be drawn to and concentrated at the insulator/graphene interface. Through reported studies, empirical evidence has been proposed that transition electrons are under nonequilibrium conditions after incident light illumination. Consequently, the optical nonlinearities rely on the carrier density at the quasi-Fermi level derived from these nonequilibrium carriers (named the quasi-equilibrium state).

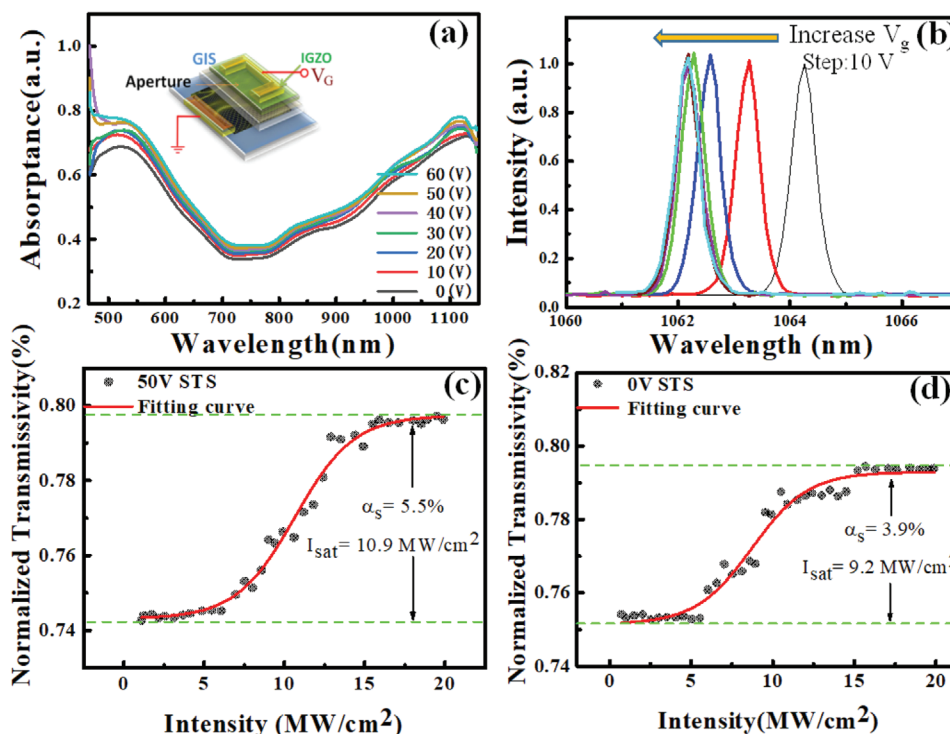


**Figure 5.** a) Optical absorption characteristic curves of GIS with N-gra SA under different gate voltages' amplitude (shown in inset images). b) Output laser spectra's blue shift under the same pump powers with increasing gate voltage amplitude from 0 to 60 V. Measuring modulation depth points of c) high and d) low voltages' amplitude of STS nanomesh-SA and their corresponding fitting curve.

The related absorbance  $a$  can be expressed as<sup>[35]</sup>

$$a = a^0 [f_1(1 - f_2) - f_2(1 - f_1)] \quad (1)$$

where  $f_1$  and  $f_2$  are the occupying probabilities of the carrier-derived Fermi level in the valence band and conduction band, respectively. This hypothesis is also a major reason why the optical absorption could be regulated by the gate voltage amplitude (negative) in previous Figure 5a and Figure S3b (Supporting Information). To explore the detailed optical-electrical interaction mechanism, the nonlinear optical properties are investigated following tunable Q-switched laser experiments.

To further prove the reliability of the gate-controlled laser system, the nonlinear transmission effects of the STS SA at different biases are measured. Figure 5c,d shows the experimental data and curves fitted by the following formula

$$T(I) = 1 - \Delta T \times e^{-I/I_{\text{sat}}} - T_{\text{ns}} \quad (2)$$

where the transmission, saturable intensity, input intensity and nonsaturable absorbance coefficient are substituted with  $T(I)$ ,  $I_{\text{sat}}$ ,  $I$ , and  $T_{\text{ns}}$ , respectively. The modulation depth is usually an important parameter that affects the performance of a Q-switched laser, which is also termed the saturable absorption coefficient.<sup>[36–38]</sup>

The numerical fitting results showed that the saturation intensities and the modulation depth of the STS SAs can be affected by the gate voltage also. Our results proved that the device exhibits a significant modulation depth change from 3.9% to 5.5% with the effect of gate voltage being due to the

increase in the carrier concentration of graphene. According to the theoretical model expression<sup>[39]</sup>

$$\tau = 3.52T_R / \Delta T \quad (3)$$

where  $\tau$  is the pulse width,  $\Delta T$  is the SA modulation depth, and  $T_R$  is the cavity round trip time. Empirical evidence has shown that the pulse width of passively Q-switched lasers has a directly positive relationship with the SA modulation depth. The previous laser's waveforms' modulation can get verification in this investigation.

As depicted in Table 1, the as-fabricated N-gra STS devices exhibit higher Pulse width modulation capability without additional tuning elements. Compared with millimeter-level fiber laser device, challenge arises in the thin film modulation along the free space light's propagation for the high power solid-state lasers. Some reported papers have demonstrated that the pulse width and wavelength can be directly tuned by electrical pumped power with or without other tuning elements. However, these devices rely on high driving pumped power and present extremely low converting output efficiency as shown in Table 1. Ultimately, our devices still present extra excellent performances at device driving power (<0.5 nW), manipulation volume ( $\mu\text{m}$ -level), high output average power (120–530 mW by gate), and optical-electrical signal's resolution ( $\approx 40$  dB, Figure S4d in the Supporting Information). In addition, the stable pulse width variation within 120 min stress measurement is recorded by a digital oscilloscope (as shown in Figure S5a in the Supporting Information). And the highest repetition rate of 390 kHz with 389 nJ maximum pulse energy was attained

**Table 1.** Performances of different tunable SA/devices Q-switched laser.

Device type	Modulation type	Saturable absorber	Pulse width	Average output power	Device modul. Power	Ref.
N-gra GIS STS	On-chip	Only N-gra	360 ns–1.05 $\mu$ s	120–530 mW	0.5 nW (10 pA)	/
Few-layer(Fl.) GIS STS	On-chip	Only Fl. Graphene	480 ns–1.05 $\mu$ s	210–530 mW	1.3	/
Few-layer(Fl.) GIM STS	On-chip	Only Fl. Graphene	800 ns–1.05 $\mu$ s	440–530 mW	50	/
Graphene SA	Fixed	Only rGO	/	600 mW	/	[7]
Graphene/Ag fiber	Directly	rGO/Ag	3.1–7 $\mu$ s	3.42 mW	91.4–158.6 mW	[22]
Graphene SA fiber	Directly	Only Graphene	2.2–5.9 $\mu$ s	9.8 mW	1.8–21.5 mW	[23]
Graphene fiber assisted Bragg grating (FBG)	Directly	Graphene assisted FBG	4.5–80 $\mu$ s	1 mW	6.5–99.7 mW	[24]
MoS <sub>2</sub> SA	Directly	MoS <sub>2</sub> assisted tunable filer	2.68–4.4 $\mu$ s	9.36 mW	/	[25]
Graphene FET fiber	On-chip	Gra.-coated nanophotonic crystal	/ (absorption modulation: 20–60%)	5 mW	300 nW	[20]
Graphene FET fiber (model switch)	On-chip	Graphene/ion-gel fiber	3.5 $\mu$ s (Q-switch) 0.432 ps (mode-lock)	3.1 mW	400 nW	[21]

(Figure S5b, Supporting Information) under gate voltage's regulation. It might allow envisioning novel heterostructure optoelectronic devices such as solid-state tunable IR detectors, optical modulators, and specific compressed laser emitters.

## 4. Conclusion

In summary, we present the fabrication process, characterization, and analysis of a graphene-insulator-semiconductor heterostructure with nanomesh SA that is feasible as an efficient modulator in Q-switched systems. Combined with a study on the electric transport and spectroscopy measurements of the vertical device with few-layered graphene and N-gra, the optical-electrical interaction mechanism is elaborated. Resulting from the shift in the Fermi level and the carrier density, the optical transmission of graphene in our device can be regulated by the gate voltage without changing the materials. Additionally, the GIS device is used as an on-chip electrically tunable nanomesh SA in the all-solid-state passively Q-switched Nd:YVO<sub>4</sub> laser system. This approach shows excellent saturable absorption characteristics with a highly controllable pulse width (from 360 ns to 1  $\mu$ s) as well as repetition frequency, while the current is limited by the dielectric ( $\approx$ 10 pA) at low driving power (<0.5 nW). It is anticipated that the development of high output power (120–530 mW) switchable laser operations will be further improved with this promising structure. In particular, applications both in Q-switching and mode-locking regimes in the future, such as distance IR measurements, projection displays, and optical modulation, will benefit from the availability of the GIS device based on graphene.

## Supporting Information

Supporting Information is available from the Wiley Online Library or from the author.

## Acknowledgements

The authors acknowledge funding from the Primary Research & Development Plan of Jiangsu Province (No. BE2016756), the National

Natural Science Foundation of China (No. 61875089, 61905116, 11374161), the Natural Science Foundation of Jiangsu Province (BK20190771), the Science and Technology innovation project of Nanjing for overseas returnees (R2019LZ01) and the Project Funded by the Priority Academic Program Development of Jiangsu Higher Education Institutions (No. 1081080015001). This work was also supported by the Topnotch Academic Programs Project of Jiangsu Higher Education Institutions (No. 1181081501003) and the Postgraduate Research & Practice Innovation Program of Jiangsu Province (SJCX19\_0308).

## Conflict of Interest

The authors declare no conflict of interest.

## Data Availability Statement

Research data are not shared.

## Keywords

actively controlled laser, GIS heterostructure, graphene nanomesh, saturable absorber

Received: September 1, 2020

Revised: February 6, 2021

Published online: March 6, 2021

- [1] S. W. Howell, I. Ruiz, P. S. Davids, R. K. Harrison, S. W. Smith, M. D. Goldflam, J. B. Martin, N. J. Martinez, T. E. Beechem, *Sci. Rep.* **2017**, *7*, 14651.
- [2] R. Yan, Q. Zhang, W. Li, I. Calizo, T. Shen, C. A. Richter, A. R. Hight-Walker, X. Liang, A. Seabaugh, D. Jena, H. G. Xing, D. J. Gundlach, N. V. Nguyen, *Appl. Phys. Lett.* **2012**, *101*, 022105.
- [3] S. Rangan, M. Kalyanikar, J. Duan, G. Liu, R. A. Bartynski, E. Y. Andrei, L. Feldman, E. Garfunkel, *J. Phys. Chem. Lett.* **2016**, *7*, 3434.
- [4] G. Zhao, J. Hou, Y. Wu, J. He, X. Hao, *Adv. Opt. Mater.* **2015**, *3*, 937.
- [5] P. Narang, L. T. Zhao, S. Claybrook, R. Sundararaman, *Adv. Opt. Mater.* **2017**, *5*, 1600914.
- [6] L. Britnell, R. V. Gorbachev, R. Jalil, B. D. Belle, F. Schedin, A. Mishchenko, T. Georgiou, M. I. Katsnelson, L. Eaves, S. V. Morozov, N. M. Peres, J. Leist, A. K. Geim, K. S. Novoselov, L. A. Ponomarenko, *Science* **2012**, *335*, 947.

- [7] R. Dai, J. Chang, Y. Li, S. Shi, H. Li, Z. Yang, R. Ding, M. Yang, *Opt. Laser Technol.* **2019**, *117*, 265.
- [8] Y. Zhao, P. Guo, X. Li, Z. Jin, *Carbon* **2019**, *149*, 336.
- [9] Y. Song, Z. Liang, X. Jiang, Y. Chen, Z. Li, L. Lu, Y. Ge, K. Wang, J. Zheng, S. Lu, J. Ji, H. Zhang, *2D Mater.* **2017**, *4*, 04501.
- [10] Q. Tian, P. Yin, T. Zhang, L. Zhou, B. Xu, Z. Luo, H. Liu, Y. Ge, J. Zhang, P. Liu, X. Xu, *Nanophotonics* **2020**, *9*, 2495.
- [11] J. Feng, X. Li, Z. Shi, C. Zheng, X. Li, D. Leng, Y. Wang, J. Liu, L. Zhu, *Adv. Opt. Mater.* **2020**, *8*, 1901762.
- [12] Y. Ge, Z. Zhu, Y. Xu, Y. Chen, S. Chen, Z. Liang, Y. Song, Y. Zou, H. Zeng, S. Xu, H. Zhang, D. Fan, *Adv. Opt. Mater.* **2018**, *6*, 1701166.
- [13] Y. Zhao, W. Wang, X. Li, H. Lu, Z. Shi, Y. Wang, C. Zhang, J. Hu, G. Shan, *ACS Photonics* **2020**, *7*, 2440.
- [14] P. L. Guo, X. Li, T. Feng, Y. Zhang, W. Xu, *ACS Appl. Mater. Interfaces* **2020**, *12*, 31757.
- [15] P. Li, Y. Chen, T. Yang, Z. Wang, H. Lin, Y. Xu, L. Li, H. Mu, B. N. Shivananju, Y. Zhang, Q. Zhang, A. Pan, S. Li, D. Y. Tang, B. Jia, H. Zhang, Q. Bao, *ACS Appl. Mater. Interfaces* **2017**, *9*, 12759.
- [16] T. Jiang, K. Yin, C. Wang, J. You, H. Ouyang, R. Miao, C. Zhang, K. Wei, H. Li, H. Chen, R. Zhang, X. Zheng, Z. Xu, X. Cheng, H. Zhang, *Photonics Res.* **2019**, *8*, 78.
- [17] F. Wang, Y. Zhang, C. Tian, C. Girit, A. Zettl, M. Crommie, Y. R. Shen, *Science* **2008**, *320*, 206.
- [18] Z. Q. Li, E. A. Henriksen, Z. Jiang, Z. Hao, M. C. Martin, P. Kim, H. L. Stormer, D. N. Basov, *Nat. Phys.* **2008**, *4*, 532.
- [19] K. S. Novoselov, A. K. Geim, S. V. Morozov, D. Jiang, M. I. Katsnelson, I. V. Grigorieva, S. V. Dubonos, A. A. Firsov, *Nature* **2005**, *438*, 197.
- [20] H. Kim, M. Lee, H. Jeong, M. S. Hwang, H. R. Kim, S. Park, Y. D. Park, T. Lee, H. G. Park, H. Jeon, *Nanoscale* **2018**, *10*, 8496.
- [21] E. J. Lee, S. Y. Choi, H. Jeong, N. H. Park, W. Yim, M. H. Kim, J. K. Park, S. Son, S. Bae, S. J. Kim, K. Lee, Y. H. Ahn, K. J. Ahn, B. H. Hong, J. Y. Park, F. Rotermund, D. I. Yeom, *Nat. Commun.* **2015**, *6*, 6851.
- [22] H. Ahmad, N. F. Azmy, S. A. Reduan, N. Yusoff, L. Bayand, M. Z. Zulkifli, K. Thambriatnam, *J. Mod. Opt.* **2020**, *67*, 1022.
- [23] R. Zhang, J. Wang, M. Liao, X. Li, P. Kuan, Y. Liu, Y. Zhou, W. Gao, *IEEE Photonics J.* **2019**, *11*, 1500310.
- [24] Y. Li, L. Gao, T. Zhu, Y. Cao, M. Liu, D. Qu, F. Qiu, X. Huang, *IEEE J. Sel. Top. Quantum Electron.* **2017**, *24*, 1.
- [25] R. I. Woodward, E. J. R. Kelleher, R. C. T. Howe, G. Hu, F. Torrisi, T. Hasan, S. V. Popov, J. R. Taylor, *Opt. Express* **2014**, *22*, 31113.
- [26] M. Zhang, X. Wang, W.-Q. Cao, J. Yuan, M.-S. Cao, *Adv. Opt. Mater.* **2019**, *7*, 1900689.
- [27] L. J. Sang, C. Seongpil, K. Sang-Mo, L. S. Yeol, *IEEE Electron Device Lett.* **2010**, *31*, 225.
- [28] X. Liu, W. Kuang, H. Ni, Z. Tao, Q. Dai, *Small* **2018**, *14*, 1800265.
- [29] H. C. Wu, C. H. Chien, *Appl. Phys. Lett.* **2013**, *102*, 062103.
- [30] A. Solieman, J. Sol-Gel, *Sci. Technol.* **2011**, *60*, 48.
- [31] D. K. Hwang, Y. T. Lee, H. S. Lee, Y. J. Lee, S. H. Shokouh, J. H. Kyhm, J. Lee, H. H. Kim, T. H. Yoo, S. H. Nam, *NPG Asia Mater.* **2016**, *8*, e233.
- [32] Z. D. Zhang, Z. S. Wang, R. Zhang, X. Y. Wu, D. J. Fu, J. R. Liu, *Nucl. Instrum. Methods B* **2013**, *307*, 260.
- [33] Y. Liu, H. Zhou, R. Cheng, W. Yu, Y. Huang, X. Duan, *Nano Lett.* **2014**, *14*, 1413.
- [34] H. Xu, Z. Zhang, Z. Wang, S. Wang, X. Liang, L.-M. Peng, *ACS Nano* **2011**, *5*, 2340.
- [35] R. N. Zitter, *Appl. Phys. Lett.* **1969**, *14*, 73.
- [36] J. Li, H. Luo, B. Zhai, R. Lu, Z. Guo, H. Zhang, Y. Liu, *Sci. Rep.* **2016**, *6*, 30361.
- [37] P. K. Cheng, C. Y. Tang, X. Y. Wang, L.-H. Zeng, Y. H. Tsang, *Photon. Res.* **2020**, *8*, 511.
- [38] P. T. Pinghua Tang, Y. T. Yue Tao, Y. M. Yuliang Mao, M. W. Man Wu, Z. H. Zongyu Huang, S. L. Shengnan Liang, X. C. Xinhang Chen, X. Q. Xiang Qi, B. H. Bin Huang, J. L. Jun Liu, C. Z. Chujun Zhao, *Chin. Opt. Lett.* **2018**, *16*, 020012.
- [39] L. Zhengqian, L. Chun, H. Yizhong, W. Duanduan, W. Jianyu, X. Huiying, C. Zhiping, L. Zhiqin, S. Liping, W. Jian, *IEEE J. Sel. Top. Quantum Electron.* **2014**, *20*, 1.